City, University of London Institutional Repository

This is the accepted version of the paper.

This version of the publication may differ from the final published version.

Design and evaluation of rotor clearances for oil injected screw compressors

David Buckney[1], Ahmed Kovacevic[2], Nikola Stosic[2]

1. Howden Compressors Ltd., R&D 2. City University, Centre for Compressor Technology

Email: david.buckney@howden.com

Abstract

Designing twin screw compressors to safely operate at higher than normal temperatures poses a challenge as the compressor must accommodate larger peak thermal distortions while maintaining efficiency at nominal operating conditions. This paper will present a case study of an oil injected compressor tested at elevated discharge temperatures with original and revised clearances. A procedure is presented to use boundary conditions derived from a chamber model to approximate component temperature distributions that are then used to predict possible thermal distortions and the resulting effect on clearance gaps. The original and revised clearance designs are evaluated and performance penalties incurred due to the modifications are discussed.

Keywords

Twin screw compressor; boundary map; rotor temperature; thermal distortion; clearances

Notation

A	centre distance between rotor axes
G	clearance gap
L, l	length
n	integer
r	polar co-ordinate radius
S	co-ordinate system origin
s	line parameter
T	temperature

X, x Cartesian co-ordinate

Y, x Cartesian co-ordinate

Z, z Cartesian co-ordinate / number of rotor lobes

β non-standard polar co-ordinate angle

γ local wrap angle

ε rotor surface parameter

θ cycle angle

λ transverse profile offset angle

φ polar co-ordinate angle / various angles

Subscripts

1   main (male) rotor

2   gate (female) rotor

c   cusp angle

I   interlobe

M   meshing angle

s   start

R   rotor

B   casing bore

w   wrap angle

local local cycle angle

Introduction

End users of twin screw compressors occasionally demand reliable compressor operation over a greater operating range than the original design envelope. If for example the allowable cooling oil temperature can be increased, this can reduce the cooling requirements and the overall plant cost. This poses a challenge as the compressor design needs to accommodate higher peak operating temperatures while maintaining efficiency at nominal operating conditions.

In one sense the clearances in oil injected machines are easier to manage than in oil free machines as temperatures are usually kept within much lower limits however the lack of timing gears and the direct rotor to rotor contact does add more complexity to clearance analysis. Rotor contact is of course necessary for one rotor to drive the other; the objective is to control precisely where it is possible for contact to occur. Best practice for direct drive clearance design ensures only rolling contact at the pitch radius of each rotor as presented by Stosic et al [1]. Deviations from nominal design clearances, whether due to manufacturing and assembly variations or due to operational distortions can result in a shift in the relative rotation between the main and gate rotors [2]: this further distorts the interlobe clearance distribution and must be considered in clearance evaluation for direct drive, oil injected compressors.

This paper will present a case study of an oil injected compressor that was tested at elevated discharge temperatures. A novel procedure is presented to estimate local clearance distortions by applying boundary conditions derived from a quasi 1-dimensional chamber model. A key stage in this procedure is the creation of a 'Rotor Boundary Map' which is unique for any given profile. The Rotor Boundary Map allows rotor to rotor and rotor to casing boundaries to be visualized on a single 2-dimensional map which allows the interaction between various compression chambers to be investigated.

Time varying boundary conditions from the non-dimensional model are mapped onto rotor and casing surfaces. The fluid boundary temperatures are time-averaged then used to estimate the local rotor and casing temperatures. Rather than apply these boundary conditions to finite element analysis [3], the thermal and clearance analysis takes a more direct analytical approach that requires some carefully considered assumptions. Heat transfer assumptions that represent the extreme case for component temperature distributions are presented. This is then used to predict possible thermal distortions and the resulting affect on clearance gaps.

Mapping fluid properties

Co-ordinate system

Figure 1 shows a representation of the casing bores and rotor axes for a twin screw machine. The global co-ordinate system, S(X,Y,Z), is located on the main rotor axis and the high pressure (HP) plane. Two additional co-ordinate systems, $S_1(x_1,y_1,z_1)$ and $S_2(x_2,y_2,z_2)$ have been located on the low pressure (LP) plane on the main and gate rotor axes respectively. This convention can be applied to any screw compressor or expander providing the helix on the main rotor is left handed.
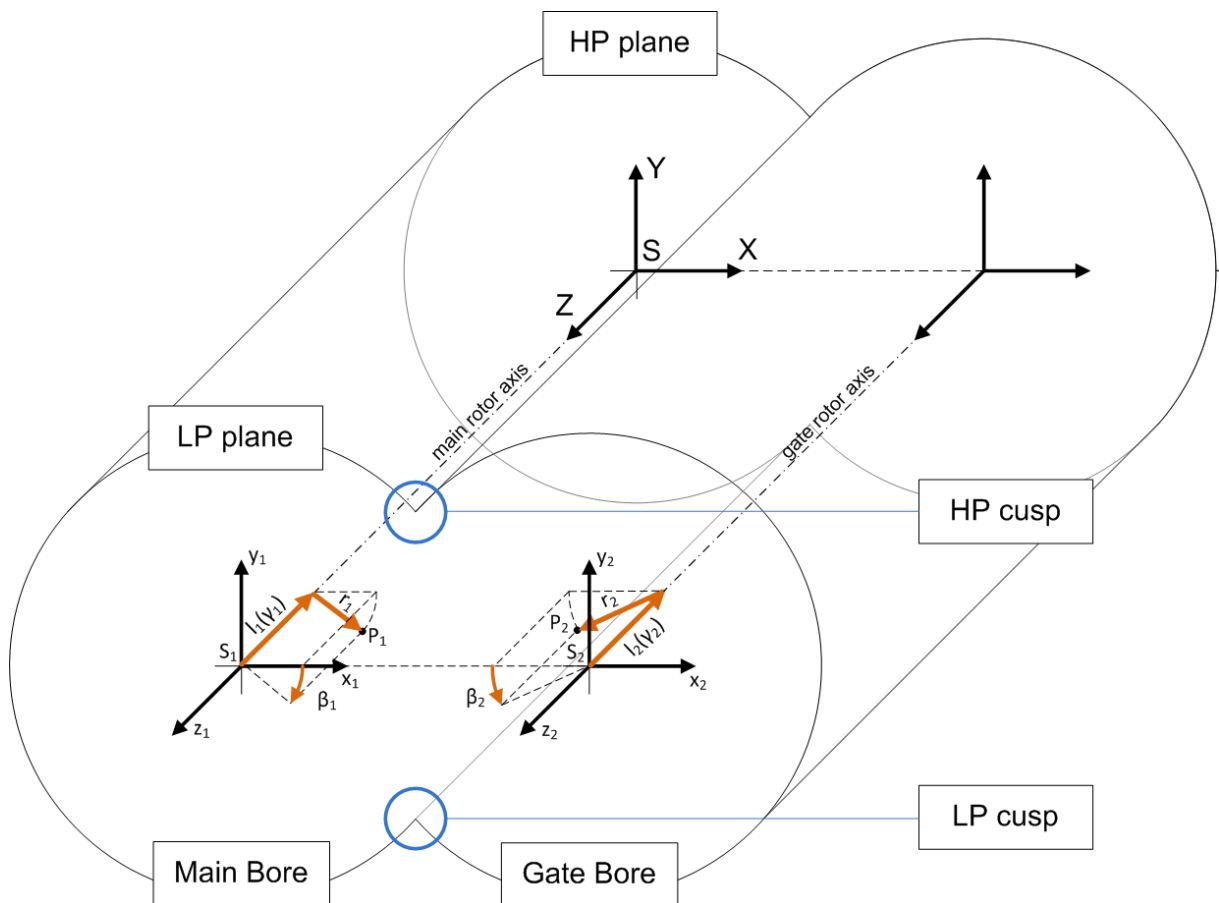

Figure 1: Co-ordinate systems and cylindrical parameters

With the cylindrical form of the rotor bores and the rotational movement of the rotors it is convenient to define points using a cylindrical co-ordinate systems located at the origins S_1 and S_2. In the standard convention for a polar co-ordinate system, (r,θ,z), the angle θ is measured counter-clockwise from the x axis and z is in the direction already defined. To simplify later equations it is preferable to define less conventional angle parameters that are aligned with the direction of rotation for each respective rotor. In addition it is easier to use an axial length parameter that is aligned from the compressor inlet to outlet. Parameters r, β and l have been defined on each co-ordinate system S_1 and S_2 as shown in Figure 1. r is the local radius, β is the angle ,measured in the same direction that the rotors rotate, and l is a measure of the axial position from compressor inlet. The length, l, can alternatively be defined by using an angular parameter, γ; this describes the local wrap angle measured from the compressor inlet. For the case of rotors with constant pitch helix the relationship is as shown in equation (1) where φ_{w1} is the main rotor wrap angle over the rotor length, l. The parameter γ always refers to the *main* rotor wrap angle. Equations (2) to (4) describe transformations from these parameters, back to the global Cartesian compressor system located at S.

$$\frac{l}{L} = \frac{\gamma}{\varphi_{w1}} \qquad (1)$$

$$X = r_1 cos(\beta_1) = -r_2 \cos(\beta_2) + A \qquad (2)$$

$$Y = -r_1 sin(\beta_1) = -r_2 sin(\beta_2) \qquad (3)$$

$$Z = L\left(1 - \frac{\gamma}{\varphi_{w1}}\right) = L\left(1 - \frac{\gamma}{\varphi_{w1}}\right) \qquad (4)$$

Rotor surfaces

Each rotor surface is replaced by a 2D surface, represented by a 2D array. The transformation between the 3D spatial domain of a rotor surface and the 2D surface computational domain is done by utilising the co-ordinate systems explained. The full 3-dimensional surface of the rotors in Figure 2 can be derived using the transverse rotor co-ordinates that are extruded along a helical path. These rotor co-ordinates are defined on the co-

ordinate system: $S_{01}(x_{01},y_{01})$; which is fixed to the main rotor as illustrated in Figure 3. The main rotor is only

partially constrained to co-ordinate system $S_1(x_1,y_1,z_1)$ as it can freely rotate about its axis, z_1. An instantaneous

point on this rotor surface could be represented globally using (X,Y,Z); or local to the respective rotor bore on

origin S_1 using (x_1,y_1,z_1) or with parameters (r_1,β_1,γ_1). The advantage of using the latter is that parameters, γ_1

and r_1 are constant, however the angle, β_1, is affected by the rotational position of the rotor, defined by the

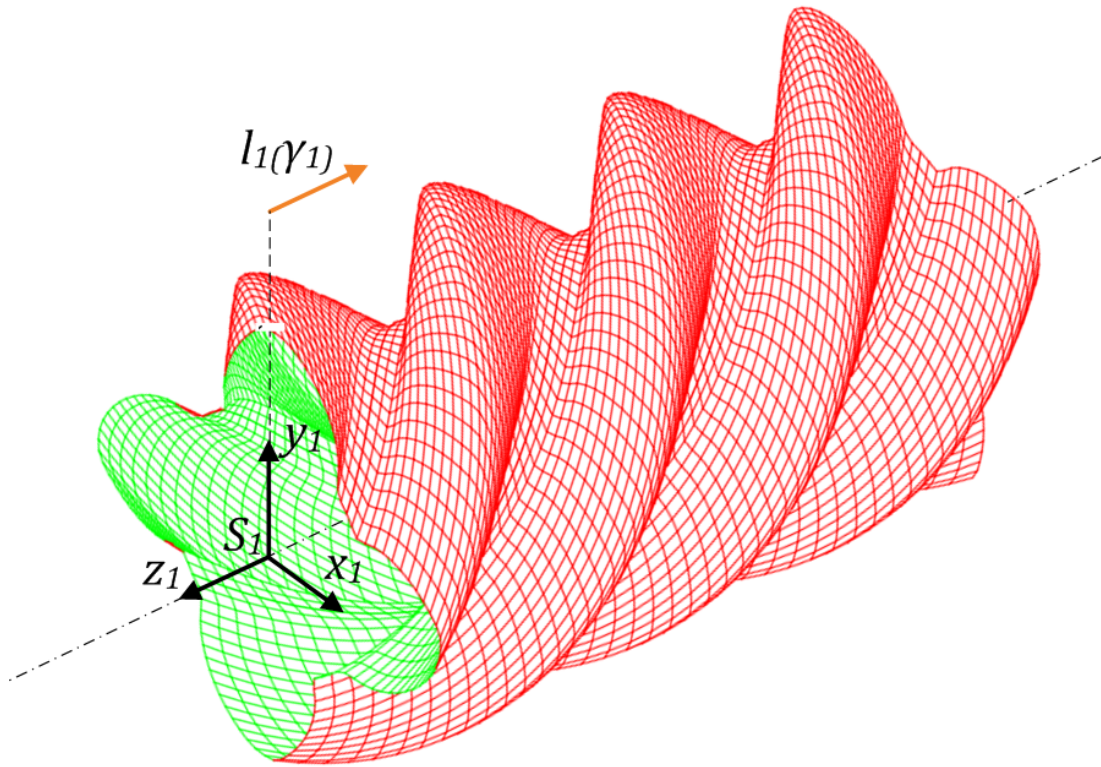cycle angle, θ.

Figure 2: Full surface of main rotor

An array has been defined to identify a surface location on a single main rotor ridge; or in the case of the gate

rotor, the corresponding flute. This array can be thought of as the surface produced by straightening out the

rotor helix and flattening the resulting surface to form a rectangle. The parameter γ represents the axial

position along the rotors and the parameter ε represents the position around the contour of the transverse profile.
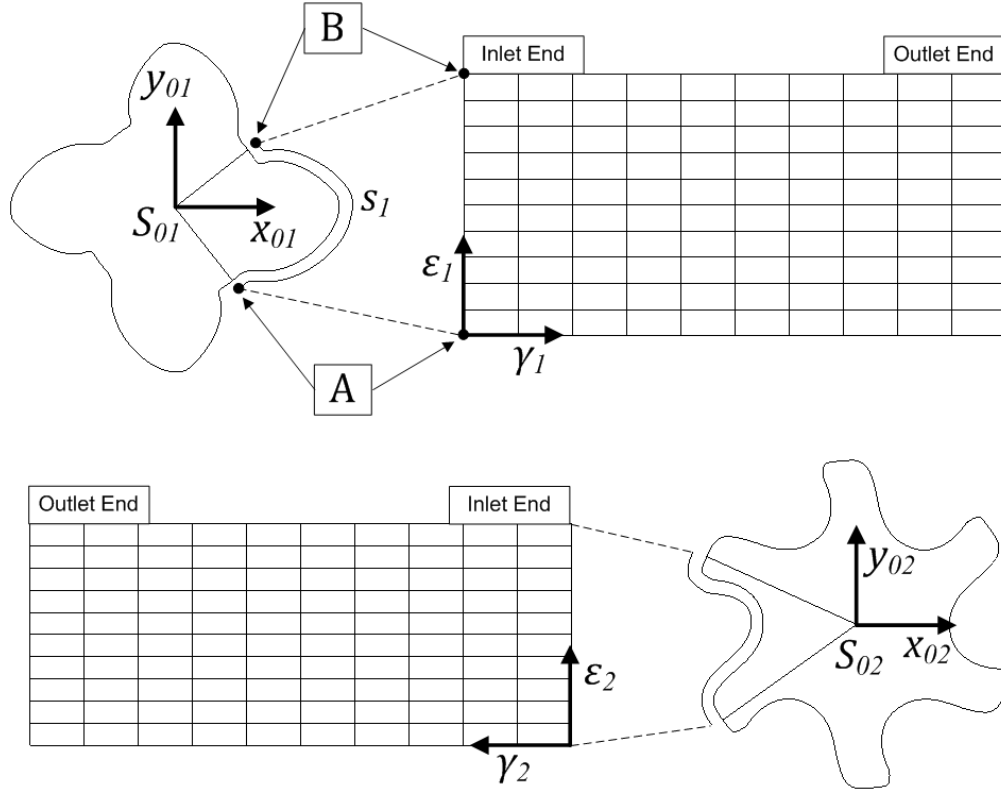

Figure 3: Rotor surface arrays

$$s_1 = \int_A^B \sqrt{dx_{01}^2 + dy_{01}^2} \qquad (5)$$

In Figure 3 the length of a curve, s_1, between points A and B can be described using equation (5). The parameter, ε, is defined as the relative position along the line, s, of the transverse rotor profile curve such that ε varies: $0 \le \varepsilon \le 1$. This is defined separately for the main and gate rotor segments. This allows any location on the rotor surface to be presented two dimensionally and independently of rotation. Each of the points on the

coordinate systems $S_{01}(x_{01}, y_{01})$ and $S_{02}(x_{02}, y_{02})$ can be described using the corresponding polar co-ordinates (r_{01}, ϕ_{01}) and (r_{02}, ϕ_{02}). These points are transverse profile constants that have a unique value for every surface position described by ε_1 or ε_2.

Cycle conventions

$$\beta_1 = (\theta - \gamma) + (-\varphi_{01}) - \varphi_{1s} \qquad (6)$$

$$\beta_2 = (\theta - \gamma)\frac{z1}{z2} + (\varphi_{02} - \pi) - \varphi_{2s} \qquad (7)$$

Equations (6) and (7) define the relationship between the angular position of a point on the rotor surface, β, and the compression cycle angle, θ. This defines how the geometry will change with time. The parameter γ, which is related to the axial position, offsets the angle to correct for the rotor helix. Since θ and γ are referenced to the main rotor, the equation for the gate rotor contains a correction for the gear ratio. The angles φ_{01} and φ_{02} are from the polar co-ordinates that describe a given point on the transverse profile. Finally, an offset is required to move the rotors to the start position when $\theta = 0$. The offsets φ_{1s} and φ_{2s} are constants for the main and gate rotors respectively. The offset is defined by the rotation of co-ordinate system S_{01} with respect to the fixed system S_1 as shown in Figure 4.
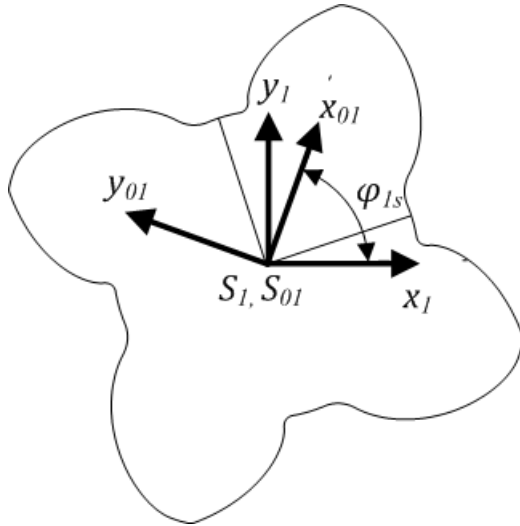
Figure 4: Main rotor offset to the start position

Rotor boundary map

On the rotor surfaces, the chamber boundaries are defined by the rotor to casing (radial sealing lines) and the rotor to rotor (interlobe sealing line). Figure 5 shows a transverse cross section of the compressor. For most of the chambers in this cross-section, the entire rotor flute (or interlobe area) is exposed to the same chamber which is separated from adjacent chambers by the radial rotor to casing sealing. During rotor to rotor contact up to three sealing points will be formed between the rotors. When this transverse section is extended to form the full 3D rotors these sealing points become complex 3-dimensional sealing lines.
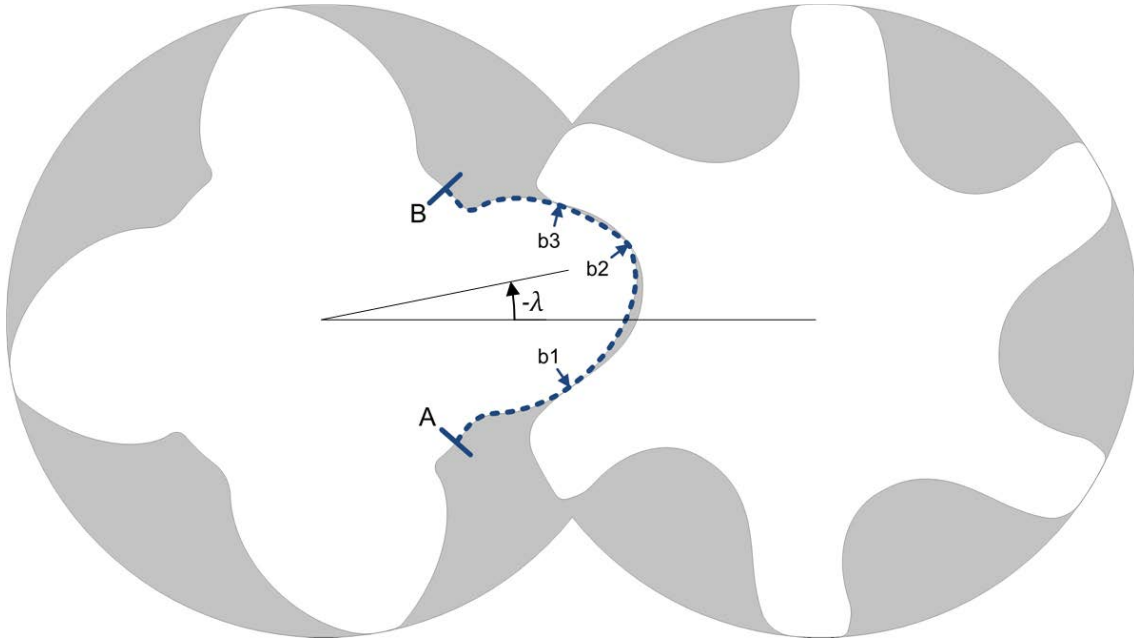
Figure 5: Transverse rotors showing boundary points

The 'Rotor Boundary Map' shown in Figure 6 is simply a way of abstracting the 3-dimensional chamber sealing boundaries in order to show what boundaries points occur around one section of the transverse rotor surface from A ($\varepsilon_1 = 0$) to B ($\varepsilon_1 = 1$) for a given position of the transverse rotor profile. The position on the rotor surface, ε, is plotted along the horizontal axis. The parameter, λ, that describes the rotor position, is plotted along the vertical axis; this parameter is detailed in Figure 5 - note that the convention for this parameter is such that the forward rotation of the rotors increases the value of λ.
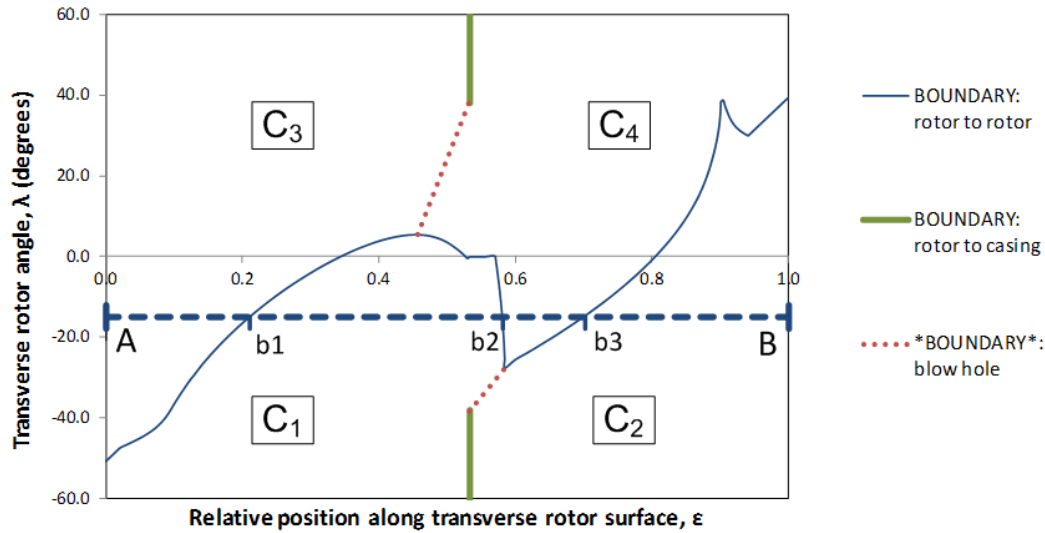
Figure 6: Rotor boundary map for main rotor

The boundaries on this map are created by plotting the radial and interlobe sealing lines with respect to ε and λ. This shows at precisely what rotor position the different boundaries come into play. The rotor to rotor boundary for the interlobe sealing line is plotted onto the boundary map by setting the profile rotation parameter λ to equal the profile meshing angle θ_M. This meshing angle is calculated for any given point of the transverse profile using the profile curve and gradient [1], [4]. The rotor to casing boundary will always occur at the same position on the profile, i.e. at the tip of the rotor; resulting in vertical lines on the boundary map. The limits of this boundary depend on the interaction between the rotor tip and the casing. In Figure 6 this boundary comes into effect when $\lambda < -\varphi_{c1}$ or $\lambda > \varphi_{c1}$; where φ_{c1} is the angle to the casing cusp measured from the main rotor.

There will be a unique boundary map for the main and the gate rotors; the form of the boundaries depends only on the transverse rotor profiles. This presentation of the rotor boundaries provides a unique way of visualising and comparing the key geometrical properties of different profiles. One thing that can be seen from

this boundary map is that the rotor to rotor boundary does not meet the rotor to casing boundary. This

discontinuity is typical of most practical rotor profile designs and results in what is known as the blow hole

leakage path. In order to explicitly define the distinct compression chambers on this map it is necessary to

introduce an artificial boundary – this was simply created by interpolating between the known boundary

conditions as shown in Figure 8: Rotor boundary map for main rotor. Four distinct quadrants, C_1 to C_4, have

now been identified that represent different compression 'chambers' on the boundary map. This allows the

rotor boundary map to be used as a reference to identify cycle exposure on the rotor surface.

Cycle exposure on surfaces

The actual boundaries that define exposure to different compression chambers are constantly shifting in time

as the rotors rotate. A procedure is needed to identify the location of the boundaries and the chamber

exposure for any given cycle angle. Equations (6) and (7) can be re-arranged in order to calculate the parameter

λ as in equations (8) and (9). For a given cycle angle, the value of λ varies when moving axially along the rotors

due to the rotor helix, described by the parameter γ. In the case of the gate rotor described by the parameters

in equation (9), λ is referenced to the rotational position of the main rotor, similarly to the way the cycle angle

θ is only referenced to the main rotor. In order to use the rotor chamber boundary map the offset should lie in

the range: $-\pi < \lambda < \pi$. To ensure the parameter λ is within this range a correction can be applied where n in an

appropriate positive or negative integer as in equation (10).

$$\lambda = \beta_1 - (-\varphi_{01}) = (\theta - \gamma) - \varphi_{1s} \qquad (8)$$

$$\lambda = \left(\beta_2 - (\varphi_{02} - \pi)\right)\frac{z2}{z1} = (\theta - \gamma) - \varphi_{2s}\frac{z2}{z1} \qquad (9)$$

$$\lambda' = \lambda + n2\pi \qquad (10)$$

For a known position of the rotor surface (ε, γ), at a known cycle angle (θ), the value of λ can now be

calculated. Knowing the location on the relevant rotor boundary map (ε, λ) it is possible to establish which

chamber quadrant (C_1, C_2, C_3 or C_4) the point lies in, this defines the 'chamber offset'. When interrogating a specific point on the rotor surface the required variable is actually the 'local cycle angle', θ_{local}. This is distinct from the 'cycle angle' θ which is effectively a 'reference cycle angle' because it only defines the cycle angle for a single 'reference compression chamber'. The cycle angle θ defines the position of the rotors while the local cycle angle θ_{local} defines cycle exposure at a specific point on the rotor surface, in a specific compression chamber. Referring back to Figure 6, the chamber offsets have been labelled on the rotor boundary map. Chamber C_4 has been set as the reference chamber.

If any adjustment is made to λ using equation (10) it is important to account for this using an additional term when calculating the local cycle angle. The general equation for calculation of the local cycle angle θ_{local} for each chamber quadrant is given in equations (11) to (14). The number added to the subscript refers to the chamber quadrant on the rotor boundary map such that θ_{local_1} is the local cycle angle in quadrant C_1.

$$\theta_{local\_1} = \theta + 2\pi + \frac{2\pi}{z1} + n2\pi \qquad (11)$$

$$\theta_{local\_2} = \theta + 2\pi + n2\pi \qquad (12)$$

$$\theta_{local\_3} = \theta + \frac{2\pi}{z1} + n2\pi \qquad (13)$$

$$\theta_{local\_4} = \theta + n2\pi \qquad (14)$$

In Figure 7 the local cycle angle, θ_{local}, has been represented by colour contours. Areas that are the same colour can be easily identified as individual compression chambers. Remember that the procedure calculates the local cycle angle over a single rotor flute, as described by the surface in Figure 3. In order to build up the full rotors the procedure was repeated after advancing the reference cycle angle θ for each lobe:

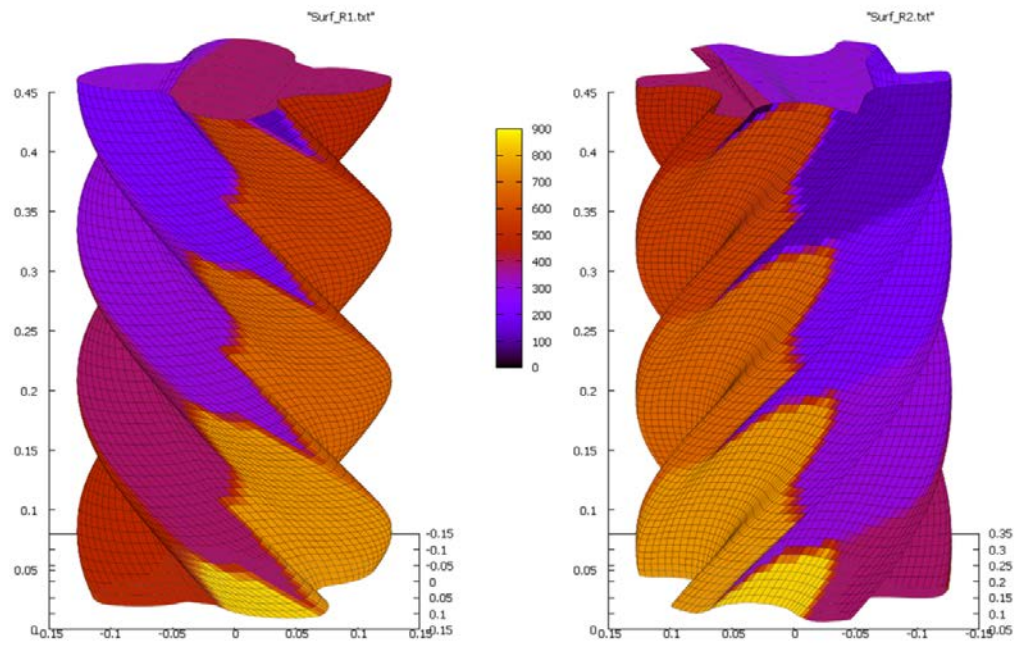$$\theta' = \theta + \frac{n2\pi}{z1} \qquad (15)$$

Figure 7: Local cycle angle plotted on 3D rotors

Some of the tiles used to produce this plot suggest a transition region across the boundary however this is an artefact introduced by averaging across nodes that fall in different chambers. All computations are done at the nodal positions therefore the calculated values will only fall within the specified local cycle angles.

Thermal analysis of clearance distortions

Fluid boundary temperature

The fluid temperature inside the compressor, assumed to be homogeneous throughout any given compression chamber, can be calculated with the use of well establish chamber models developed for twin screw compressors **[5]**. Once the local cycle angle is known at a given location on the rotor surface for a given cycle angle it is straightforward to map the corresponding instantaneous fluid properties from a chamber model onto the rotor surfaces. This instantaneous fluid boundary temperature can be described as a function of the position on the rotor surface and the cycle angle: $T_{R1}(\varepsilon_1,\gamma,\theta)$. In equation (16) this temperature has been time averaged by integrating the temperature at each surface location over one full rotation of the rotor. In equation (17) the temperature over each transverse cross section of the surface has been averaged around the transverse profile. Once averaged in this way, the fluid boundary temperature for each respective rotor varies only with axial position along the rotors, described by the parameter γ.

$$T_{R1}^*(\varepsilon_1,\gamma) = \frac{1}{2\pi}\int_0^{2\pi} T_{R1}(\varepsilon_1,\gamma,\theta)\,d\theta \qquad (16)$$

$$T_{R1}^{**}(\gamma) = \int_0^1 T_{R1}^*(\varepsilon_1,\gamma)\,d\varepsilon_1 \qquad (17)$$

A procedure for calculation of the instantaneous fluid temperature at a point on the surface of the casing bores (B_1 and B_2) can be applied similarly as for the rotors; in this case the chambers are only defined by the radial sealing boundary, greatly simplifying the procedure. The surface on the bore is described by the parameters β and γ so the instantaneous fluid boundary temperature at each point on the bores can be described with the functions: $T_{B1}(\beta_1,\gamma,\theta)$ and $T_{B2}(\beta_2,\gamma,\theta)$. In order to time average the casing exposure the limits of integration depend where the point is on the casing surface and covers a range defined by the distance between one lobe and the next: $2\pi/z1$. Equation (19) is used to time average the temperature at the main rotor bore B_1. In equation (19) the temperature has been averaged over a transverse section of *both* bores B_1 *and* B_2. The limits of integration are defined using the cusp angle for each bore, φ_{c1} and φ_{c2}.

$$T_{B1}^*(\beta_1, \gamma) = \int_{\theta(\beta_1,\gamma)}^{\theta(\beta_1,\gamma)+\ 2\pi/z1} T_{B1}(\beta_1, \gamma, \theta)\ d\theta \qquad\qquad (18)$$

$$T_{B1,B2}^{**}(\gamma) = \frac{\int_{\varphi_{C1}}^{(2\pi-\varphi_{C1})} T_{B1}^*(\beta_1,\gamma)\ d\beta_1}{4(\pi-\varphi_{C1})} + \frac{\int_{\varphi_{C2}}^{(2\pi-\varphi_{C2})} T_{B2}^*(\beta_2,\gamma)\ d\beta_2}{4(\pi-\varphi_{C2})} \qquad\qquad (19)$$

Heat transfer assumptions

The realism of thermal analysis depends on accurate representation of the compressor geometry as well as appropriate boundary conditions describing the compressor interactions with its surrounding. This generally requires the use of 3D numerical methods such as finite element method (FEM). More realism generally comes at the expense of more complexity with greater computational cost and time. Despite additional complexity, use of some assumptions or empirical factors [6] is difficult to avoid. The following procedure is not intended to calculate the *actual* local temperature on any given component, rather the average fluid boundary temperatures will be used to provide a good estimation of the *maximum* temperature that the compressor components can reach.

Conduction along the axial length of the rotors is neglected. This means there is no heat transfer from the hot end to the cold end of the rotor and no heat transfer along the rotor shafts to or from the bearings. This results in a local maximum rotor temperature which is probably higher than the actual maximum. A uniform temperature is assumed over the transverse section of each component. The component temperature is assumed to be the same as the average fluid boundary temperature defined in equations (17) and (19).

Approximating thermal distortions

The change in the local interlobe gap is calculated using a 2-dimensional approach. Figure 8 shows the known location of a local sealing point under investigation. Thermal distortions are evaluated analytically for the: main rotor co-ordinates x_1 and y_1; gate rotor co-ordinates x_2 and y_2; and the distance between axes, A, corrected by the interpolation between the thermal growth of the casing at suction and discharge faces. The close up of the

intelobe gap in Figure 8 shows the transverse clearance gap, G_{IT}, and it's components, G_{Ix} and G_{Iy}. The change in the gap is related to changes in the rotor and casing dimensions as described in equations (20) and (21). Equation (22) states approximations that allow further simplification of the analysis by eliminating the need to use the gate rotor dimensions. Once known, the *transverse* gap can be used to determine the *normal* gap [7].
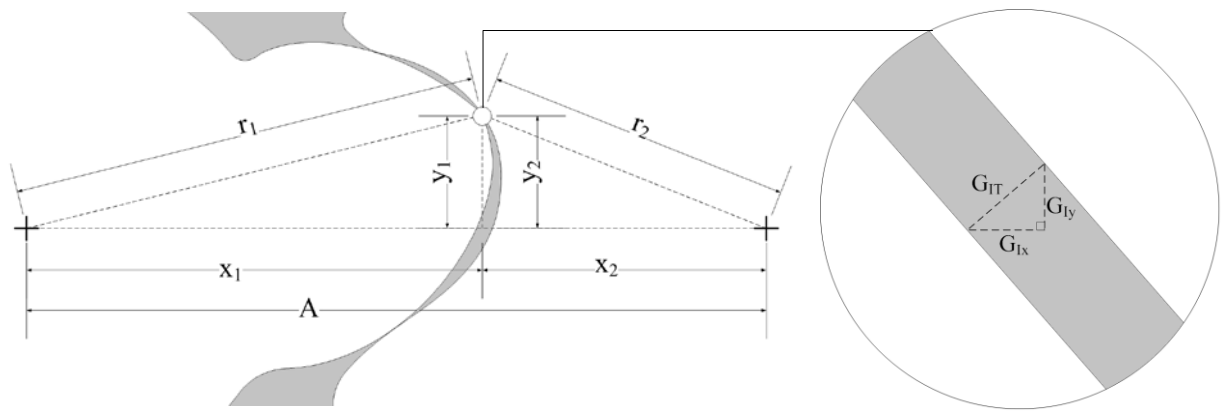

Figure 8: Local definition of intelobe gap

$$\Delta G_{Ix} = -\Delta x_1 - \Delta x_2 + \Delta A \qquad (20)$$

$$\Delta G_{Iy} = \left(\frac{(r_1 - r_{1w})}{|(r_1 - r_{1w})|}\right)(|\Delta y_2| - |\Delta y_1|) \qquad (21)$$

$$x_2 \sim (A - x_1); \quad y_2 \sim y_1 \qquad (22)$$

Case study

Evidence of rotor contact

The compressor under investigation is a Howden WCVTA510/193/26; this is currently the largest Howden compressor with rotors just over 510mm in diameter. In this case the compressor has a built in volume ratio of 2.6. In addition to air testing at the contract pressure ratio and temperature this compressor was tested at an elevated discharge temperature by increasing the pressure ratio to 11 and then limiting injection oil cooling by increasing oil temperature and restricting flow. Due to the power restriction on the testing of this large

compressor the speed was reduced from the contract speed of 1400rpm to 750rpm during this overload

testing. After testing at up to a discharge temperature of 120°C (from suction at 20°C), tear down inspection

revealed that rotor to rotor contact had occurred at the root of the main rotor as highlighted in Figure 9.
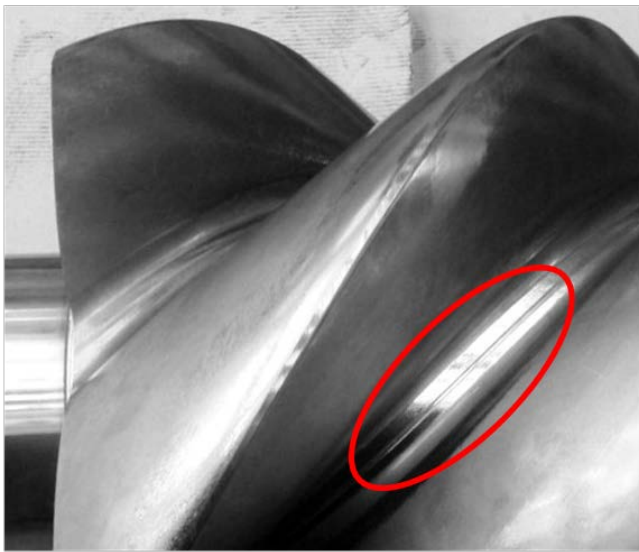

Figure 9: Main rotor showing rooting after testing at 120 degrees C

The type of contact observed and the fact that this standard compressor had not presented any problems while

operating within normal temperature limits points to thermal distortion of the rotors being the most likely

cause of this rotor contact. Based on these test findings a revised interlobe clearance design was proposed. The

revised clearance design was implemented on a different compressor at a later date and though teardown

inspection revealed some localised rotor contact, related to the tip sealing strip, there was no contact over the

main part of the root and the clearance modification was approved for further use. To better understand the

clearance behaviour the procedure outlined in this paper was applied to predict component temperatures and

thermal distortions.

Rotor and casing temperature

The overload test condition, with a discharge temperature of 120° C was modelled to determine how the temperature varied throughout the compression cycle for that particular duty. All modelling was done to replicate the test conditions where the overload discharge temperature was achieved by compressing air. The fluid temperature from the compression cycle was mapped onto the surfaces of the rotors and the casing bores. Figure 10 shows the temperature of the fluid boundary on the main and gate rotor surfaces. The left image shows the instantaneous fluid temperature for a particular rotor position. In the right hand image these instantaneous temperatures have been averaged using equations (16) and (17).
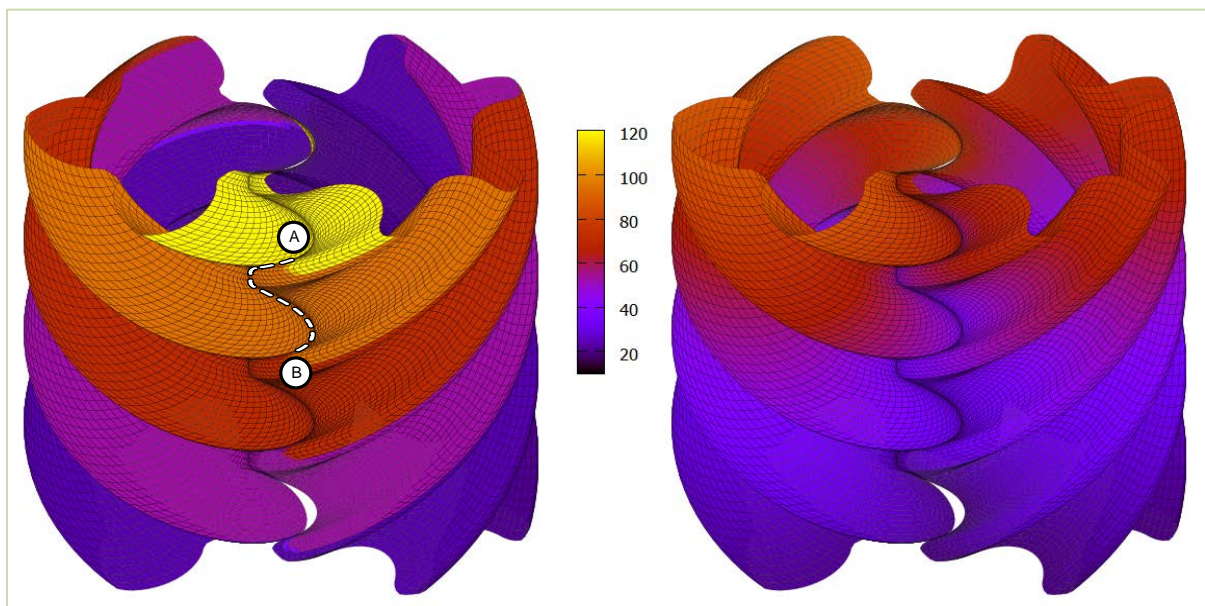

Figure 10: Instantaneous (left hand side) and averaged (right hand side) fluid boundary temperature

Table 1: Average fluid boundary temperature across the outlet plane.

Component Description	Temperature (°C)
Main rotor	86.8
Gate rotor	73.2
Casing	69.4

Figure 10 shows that the peak temperature occurs at the outlet plane of the rotors therefore the analysis will be based on the average fluid boundary temperatures at outlet; these are presented in Table 1. It is clear that the averaged fluid boundary temperatures at critical locations on the compressor are actually much lower than the peak fluid discharge temperature of 120°C.

Clearances

Figure 11 shows the magnitude of normal clearances mapped onto each of the rotors as vectors normal to the transverse rotor curve. This approach is very intuitive and clearly shows how clearances relate to difference areas on the rotor profiles, however magnifying the vectors to show the clearance distribution in more detail quickly distorts the apparent clearance gap due to the curvature of the profiles. On the other hand, plotting local clearances on a linear axis such as the relative position on the sealing line makes it difficult to determine where the clearances actually occur on the rotors.
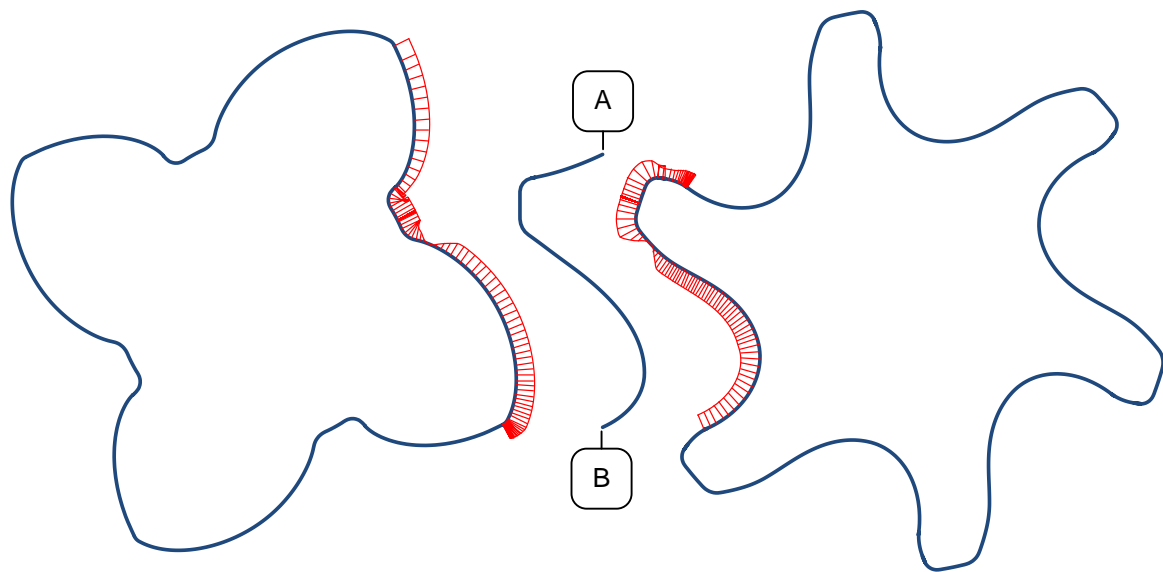

Figure 11: Transverse cross-section of main and gate rotors showing local interlobe clearances
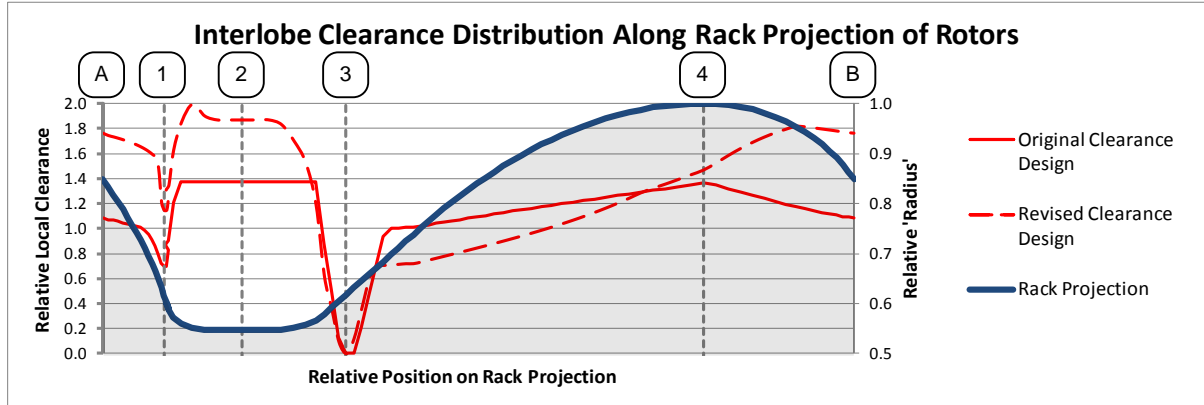
Figure 12: Interlobe clearance distribution along rack projection of rotors comparing original and revised clearance designs.

Figure 12 shows the clearance distribution in an alternative form where the local clearances are plotted against a rack projection. Line AB represents the conjugate rack, common to both rotors. The horizontal axis is the arc length of the rotor pitch circle; this is the axis along which the rack would translate. Vertical lines have been added along this axis to identify key points along the length of this sealing line projection, details of which are provided in Table 2. The limits of this rack segment are the beginning and end of the sealing line for a single compression chamber, as previously highlighted in Figure 11. The secondary axis shows the relative radius on the rack to give a better indication of where local clearances are located. In this way, the magnitude of the local clearances can be simply graphed against the somewhat familiar shape of the rack.

Table 2: Key clearance locations

Location on rack	Description
A	Limit of sealing line for single chamber
1	Pitch circle on the trailing side of the main rotor
2	Root of main rotor / tip of gate rotor
3	Pitch circle on the leading side of the main rotor

4	Tip of the main rotor / root of the gate rotor
B	Limit of sealing line for single chamber

The original and revised clearance distributions are both shown in Figure 12. In all cases the relative rotation between the rotors is adjusted in order to provide zero clearance at location 3: the pitch radius on the round side of the rotors. This is where the driving force is transferred from the main to the gate rotor. In the revised clearance design the main difference is that the clearance in the main rotor root has been increased and to a lesser extent also at the main rotor tip. Notice that the clearance on the round flank of the rotors (between locations 3 and 4) has actually been decreased on the revised clearance design – this clearance will not significantly reduce during operation because the gap is maintained due to the nearby contact at the pitch point (location 3), therefore this clearance was deemed to be unnecessarily large. Conversely, on the straight flank (from 4 to B, and from A to 1) the gap is adversely affected by thermal distortions at location 3 which are transferred over to the straight flank. Therefore it was necessary to increase the clearances on the straight flank. To quantify how these clearance changes impact the leakage area through the interlobe gap the local clearances where integrated over the length of the 3D sealing line. The total leakage area is 108.5mm^2 for the original design is and 142.7mm^2 for the revised design, an increase of 31.5%.

Clearance distortion results

The following results show the predicted operational clearance distributions for the original and revised designs in Figure 13 and Figure 14 respectively. The temperature increase in both the rotors and casing shown in Table 1 would result in little net change in the operational clearances, this case has been presented with the longer dashed lines on each figure, the trend is not far off the original clearance. A second case has also been presented where the rotors do not move apart due to casing thermal expansion. This case is likely in the event that sudden temperature changes cause the rotors to heat up faster than the casing or alternatively the outlet

end bearings might be situated remotely from the rotor outlet plane in a location where the casing temperature is much lower than estimated in Table 1. The distance between the two dashed curves for the different operational scenarios results in a large band of uncertainty but it does serve to highlight 1) where rotor contact is most likely to occur for a given clearance design, and 2) where clearances can be further reduced without compromising reliability.
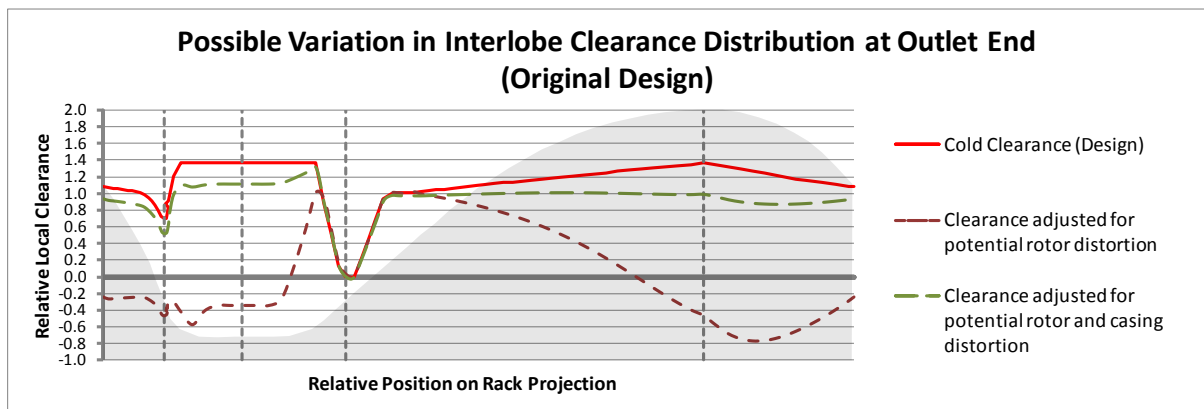

Figure 13: Possible variation in interlobe clearance distribution at outlet end (original design)
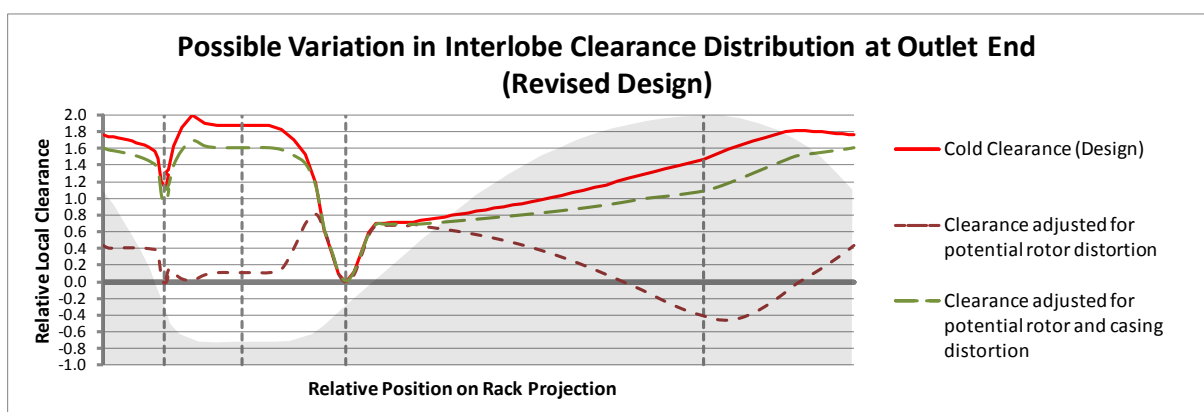

Figure 14: Possible variation in interlobe clearance distribution at outlet end (revised design)

This analysis supports the suitability of the revised clearance in the root of the main rotor which shows contact cannot now occur there due to thermal distortion alone. The chance of contact at the tip of the main rotor has

been significantly improved however the analysis suggests contact is still possible under extreme circumstances.

Performance predictions

The models were also run at the nominal air test duty which is closest to the designed operating conditions: with a speed of 1400rpm, a pressure ratio of 5 and a discharge temperature maintained at approximately 90°C. The modelled deviation in the volume flow due to the revised design is compared with the deviation measured on test in Table 3.

Table 3: Performance penalty with revised interlobe clearance at pressure ratio of 5

	change in volumetric flow
Modelled	-0.5%
Measured on Test	-1.7%

The difference between the model result and the test result was higher than expected suggesting that the model is slightly underestimating the effect of leakages through the interlobe gap. Unfortunately as the test results were obtained using two different compressors the effect of other manufacturing and assembly tolerances can't be ruled out for the test results. Importantly, the resulting change in flow on test was small enough that the compressor was still within normal operating tolerances in both cases. With the reduced flow there was a similar reduction in shaft power so there was very little change in the overall efficiency. It is to be expected there would be some detrimental effect on performance at the nominal operating condition by increasing the rotor clearances to allow the compressor to operate at higher, non-standard, operating temperatures. This same design approach could be applied to investigate how far clearances could potentially be reduced for performance optimisation over a narrow operating band.

Conclusions

A procedure has been presented to map thermodynamic results from a lumped parameter chamber model onto discrete rotor surfaces. The rotor boundary map used in this procedure provides a unique way of visualising and comparing the key geometrical properties of different profiles. Fluid boundary conditions calculated with the aid of the rotor boundary map can be used for further analysis of compressor components. For example, to provide initial boundary conditions for more specialised finite element analysis (FEA) or computational fluid dynamics (CFD).

Surface boundary conditions were used to estimate the temperature distribution of the compressor rotors and casing that result in the largest feasible peak temperatures during normal operation. Local variations in clearances, due to thermal distortions, have been approximated analytically. This provides valuable data about where and when in the compression process clearances are inadequate for a given compression application. Integrating this information into the rotor design process allows a more optimised balance between reliability and compressor performance.

Two interlobe clearance designs have been analysed to evaluate how suitable they are for operation at an elevated rotor discharge temperature of 120°C in an oil injected compressor with direct rotor drive. While there is a fairly large uncertainty on the predicted clearance deviations the results do confirm that the revised clearances should prevent rotor to rotor contact at the root of the male rotor. This is where contact was initially present on test, and later shown to be alleviated due to the revised clearance design.

Performance test results suggest that the increase in interlobe clearance has resulted in a 1.7% drop in flow however the overall flow was still within normal test tolerances. The change in flow predicted by the model was different from that measured on test.

References

1. Stosic N, Smith IK and Kovacevic A. *Screw Compressors: Mathematical Modelling and Performance Calculation.* UK. 2005.

2. Sauls J, Powell G, and Weathers B. Thermal deformation effects on screw compressor rotor design. In International Conference on Compressors and their Systems, September 10, 2007 - September 12, 2007, pp. 159-168 (Chandos Publishing, London, United kingdom).

3. Sauls J, Powell G, and Weathers B. Transient thermal analysis of screw compressors part I - Development of thermal model. *VDI Berichte* , 2006, , 19-29.

4. Litvin FL and Fuentes A. *Gear Geometry and Applied Theory.* 2004.

5. Hanjalic K and Stosic N. Development and optimization of screw machines with a simulation model - Part II: thermodynamic performance simulation and design optimization. *J Fluids Eng Trans ASME* , 1997, 119, 664-670.

6. Hsieh SH, Shih YC, Hsieh W, Lin FY, and Tsai MJ. Calculation of temperature distributions in the rotors of oil-injected screw compressors. *International Journal of Thermal Sciences* , 2011, 50, 1271-1284.

7. Holmes C. *A study of screw compressor rotor geometry leading to a method for inter-lobe clearance measurement.* Huddersfield Polytechnic. 1990. .